Carbon-based primary productivity modeling with vertically resolved photoacclimation

T. Westberry,[1] M. J. Behrenfeld,[1] D. A. Siegel,[2] and E. Boss[3]

Received 3 August 2007; revised 8 January 2008; accepted 8 February 2008; published 13 June 2008.

[1] Net primary production (NPP) is commonly modeled as a function of chlorophyll concentration (Chl), even though it has been long recognized that variability in intracellular chlorophyll content from light acclimation and nutrient stress confounds the relationship between Chl and phytoplankton biomass. It was suggested previously that satellite estimates of backscattering can be related to phytoplankton carbon biomass (C) under conditions of a conserved particle size distribution or a relatively stable relationship between C and total particulate organic carbon. Together, C and Chl can be used to describe physiological state (through variations in Chl:C ratios) and NPP. Here, we fully develop the carbon-based productivity model (CbPM) to include information on the subsurface light field and nitracline depths to parameterize photoacclimation and nutrient stress throughout the water column. This depth-resolved approach produces profiles of biological properties (Chl, C, NPP) that are broadly consistent with observations. The CbPM is validated using regional in situ data sets of irradiance-derived products, phytoplankton chlorophyll:carbon ratios, and measured NPP rates. CbPM-based distributions of global NPP are significantly different in both space and time from previous Chl-based estimates because of the distinction between biomass and physiological influences on global Chl fields. The new model yields annual, areally integrated water column production of $\sim$52 Pg C a^{-1} for the global oceans.

Citation: Westberry, T., M. J. Behrenfeld, D. A. Siegel, and E. Boss (2008), Carbon-based primary productivity modeling with vertically resolved photoacclimation, *Global Biogeochem. Cycles*, *22*, GB2024, doi:10.1029/2007GB003078.

1. Introduction

[2] An understanding of phytoplankton photosynthetic production in the ocean and its role in carbon cycling is fundamental to contemporary climate science and has been broadened tremendously by the advent of ocean color remote sensing. Our understanding of the underwater light field has similarly increased under the umbrella of interpreting ocean color related data [*Gordon and Morel*, 1983; *McClain et al.*, 1998]. Realizing the benefits of these developments on net primary production (NPP) estimates, however, has been hampered by the inadequate treatment of physiological variability [*Behrenfeld and Falkowski*, 1997; *Siegel et al.*, 2001; *Behrenfeld et al.*, 2002]. This inadequacy does not so much reflect a lack of understanding of phytoplankton physiology, as sophisticated models of algal photophysiology, nutrient uptake, and growth exist for a variety of conditions [e.g., *Geider et al.*, 1996, 1998; *Flynn*, 2001], but rather, in parameterizing these processes at regional to global scales in terms of easily accessible quantities.

[3] It has long been known that phytoplankton cellular chlorophyll (Chl) concentrations are extremely plastic, responding to changes in growth irradiance (photoacclimation), nutrient status, taxonomy, and other environmental stressors [*Laws and Bannister*, 1980; *Geider*, 1987; *Falkowski and La Roche*, 1991]. Because of this plasticity, Chl is often a poor proxy for phytoplankton biomass, but remains the primary field metric of biomass in lieu of a simple alternative. It is the phytoplankton carbon biomass (C) that more appropriately describes algal standing stocks, especially as it relates to NPP which is a rate of carbon turnover (and not Chl). Further, the two quantities are linked through the Chl:C ratio, a quantity that has a wide range of variability and is often mistreated in ecosystem models [*Geider*, 1987; *MacIntyre et al.*, 2002].

[4] Remote sensing of C standing stocks for different components of marine ecosystems is a recent development. Estimates of total particulate organic carbon (POC) have been made from remote sensing measurements by relating the amount of scattered light in the water column to the particle load [*Loisel et al.*, 2001; *Stramski et al.*, 1999]. Similarly, particle scattering has been related to phytoplankton-specific quantities as well. *Behrenfeld and Boss* [2003] evidenced a relationship between Chl and the particulate beam attenuation coefficient, c_p, which is most sensitive to particles with diameters of $\sim$0.5–20 μm in size [*Stramski and Kiefer*, 1991] and generally overlaps the size distribution of phyto-

[1]Department of Botany and Plant Pathology, Oregon State University, Corvallis, Oregon, USA.
[2]Institute for Computational Earth System Science, University of California, Santa Barbara, California, USA.
[3]School of Marine Sciences, University of Maine, Orono, Maine, USA.

0886-6236/08/2007GB003078$12.00

plankton in the ocean. When combined with measurements of Chl, the Chl:c_p ratio can closely track changes in photosynthetic competency [*Behrenfeld and Boss*, 2003, 2006]. Unfortunately, c_p is not currently estimated from satellite ocean color, but an alternative may exist in the particulate backscatter coefficient, b_{bp} [*Behrenfeld et al.*, 2005].

[5] The simultaneous satellite retrieval of b_{bp} and Chl provides a means for investigating fundamental differences in the behavior of phytoplankton Chl and C in both space and time. It is not unexpected that the two will often be out of phase with one another, and many examples exist demonstrating this decoupling. In the vertical dimension, a common feature throughout much of the global ocean is a subsurface Chl maximum [*Cullen*, 1982; *Kitchen and Zaneveld*, 1990]. Although this feature can result from an accumulation of biomass at depth [e.g., *Winn et al.*, 1995], it most often reflects the increase in intracellular Chl concentration from photoacclimation [e.g., *Cullen*, 1982]. Similarly, seasonality in surface Chl of tropical stratified oceans is not matched by concurrent changes in C, and in temperate, seasonal ocean basins (e.g., the North Atlantic) the increase and peak of both Chl and C biomass can be offset as well [*Winn et al.*, 1995; *Behrenfeld et al.*, 2005]. In each of these cases, the mismatches in time and space between Chl and phytoplankton C proxies are due to the combined effects of phytoplankton growth and physiological adjustment, and thus, the ability to distinguish between the two processes is critical.

[6] *Behrenfeld et al.* [2005] recently introduced a novel approach to modeling NPP that addressed many of the above-mentioned issues. Information contained in ocean color reflectance spectra on particulate backscattering was transformed to direct estimates of C. The Chl:C ratio reflects photoacclimation and nutrient stress and has been shown to track phytoplankton physiology both in the laboratory and in the field [*Behrenfeld and Boss*, 2003; *Behrenfeld et al.*, 2005]. Consequently, Chl:C was related to the phytoplankton community growth rate, μ, and NPP. Here, we build upon these ideas by more accurately characterizing the ambient light field with respect to wavelength, allowing direct calculation of photoacclimation throughout the water column and relieving the fixed vertical structure of production originally imposed [*Behrenfeld and Falkowski*, 1997]. An additional term is included which represents the phytoplankton physiological state under no-growth conditions ($\mu = 0$) [*Geider*, 1987]. Last, inclusion of a climatological nitracline allows for relaxation of nutrient stress with depth when applicable. The result is the ability to calculate fully resolved vertical profiles of phytoplankton Chl, C, growth rate, and NPP which are broadly consistent with field data. Direct comparisons to regionally representative field measurements are made providing model validation, and the resulting global patterns are described.

2. Methods

2.1. Data Sources

[7] Global, gridded monthly fields of photosynthetically available radiation (PAR) and diffuse attenuation at 490 nm, $K_d(490)$, were provided by the OceanColor Web (http://oceancolor.gsfc.nasa.gov) and are calculated from Sea-Viewing Wide Field-of-View Sensor (SeaWiFS) measurements for the period January 1998 to December 2004. All of the products are standard level 3 monthly composites (Reprocessing 5.1) with a spatial resolution of ~9 km at the equator. SeaWiFS normalized water leaving radiances, $nL_w(\lambda)$, were also inverted to estimate Chl and the particulate backscatter coefficient at 443 nm, $b_{bp}(443)$ [*Maritorena et al.*, 2002]. Mixed layer depth (MLD) was provided by Fleet Numerical Meteorology and Oceanography Center daily data assimilated model output at a resolution of $1^\circ \times 1^\circ$ [*Clancy and Sadler*, 1992]. MLD was defined as the depth at which temperature change was 0.5°C cooler than the surface temperature and binned to monthly averages. Nitracline depths (z_{NO3}) were calculated from monthly climatological nutrient fields reported in the World Ocean Atlas [*Conkright et al.*, 2002] and defined as the depth where nitrate + nitrite exceeded 0.5 μM. All global input fields were interpolated to a 1° grid to match the most coarsely estimated and least well-constrained variables, MLD and z_{NO3}. (See Table S1 for a summary of all input data fields used in our analysis and their original spatial and temporal resolutions.[1])

[8] In situ measurements used for validation were from time series programs in the Pacific (Hawaii Ocean Time-series (HOT)) and Atlantic (Bermuda Atlantic Time-series Study (BATS)). Both programs are ongoing, and data collection protocols and broad overviews are available [*Karl and Lukas*, 1996; *Karl et al.*, 2001; *Steinberg et al.*, 2001]. NPP data from the HOT and BATS program were based on dawn-to-dusk in situ ^{14}C incubations from the surface to 175 m (140 m for BATS). Chromatographic Chl concentrations in the upper 200 m of the water column from the BATS site and radiometric data collected in conjunction with the BATS were also used for model comparison [*Siegel et al.*, 2001]. Spectral diffuse attenuation, $K_d(\lambda)$, is calculated as the slope of the log-transformed downwelling irradiance profiles as described by *Mueller et al.* [2002]. Additional data sets from the HOT and BATS sites of *Prochlorococcus* cellular fluorescence determined by flow cytometry were reproduced with permission as by *Winn et al.* [1995] and *Durand et al.* [2001].

2.2. Chlorophyll, Particulate Backscatter, and Phytoplankton Carbon

[9] SeaWiFS ocean color reflectance spectra were inverted using the method of *Maritorena et al.* [2002]. The inversion method is a nonlinear minimization that solves for three unknown quantities (Chl, $b_{bp}(443)$, and the absorption by colored dissolved and detrital matter at 443nm, $a_{cdm}(443)$) which together best reproduce the satellite-measured spectral reflectance.

[10] Measurements of scattering (b_{bp} and c_p) have been related to total particulate organic carbon (POC) for some time [*Bishop*, 1999; *Stramski et al.*, 1999; *Babin et al.*, 2003]. The relationship with phytoplankton carbon (C), however, is a bit more tenuous, as C is difficult to measure, and therefore, no direct relationships can be derived. A number of independent constraints and assumptions can be

[1] Auxiliary materials are available in the HTML. doi:10.1029/2007GB003078.

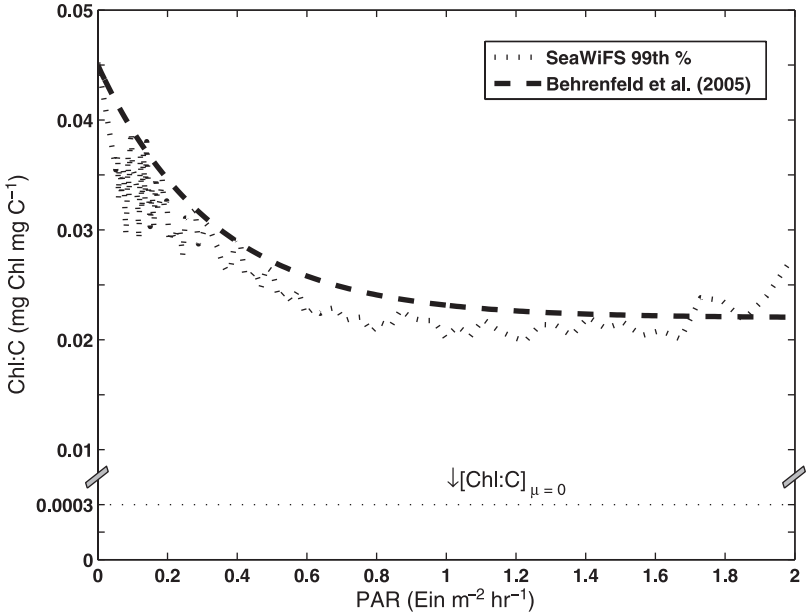

Figure 1. Relationship between Chl:C and irradiance (Ein m^{-2} h^{-1}). Dotted curve represents 99th percentile of Chl:C distribution at discrete lognormally distributed bins in associated monthly median mixed layer irradiances. Heavy dashed curve is relationship used by *Behrenfeld et al.* [2005] and in this work. Also shown is invariant Chl:C when $\mu = 0$ (designated as $\frac{Chl}{C}_{\mu=0}$ in text). Note: 1 Ein = 1 mole photons.

used to link light-scattering indices and C. In the ocean, the particulate beam attenuation coefficient, c_p, is most sensitive to particles in the size range of ~0.5–20 μm which overlaps the size range of most phytoplankton, so it is reasonable to expect a relationship with phytoplankton C, perhaps even more so than with POC [*Behrenfeld and Boss*, 2003, 2006]. According to Mie theory, particulate backscattering, b_{bp}, is more sensitive than c_p to the presence of small nonalgal particles [*Stramski and Kiefer*, 1991]. However, there are many indications that Mie theory may be inappropriate for modeling backscattering of diverse particle assemblages including phytoplankton [*Vaillancourt et al.*, 2004; G. Dall'Olmo et al., Direct contribution of phytoplankton-sized particles to optical backscattering in the open ocean, submitted to Limnology and Oceanography, 2008, in review]. And perhaps more importantly, the highly conserved nature of the particle size spectrum in the ocean and the fact that most particle assemblages in the open ocean covary with phytoplankton abundance can allow b_{bp} to track C to first approximation.

[11] Following *Behrenfeld et al.* [2005], $b_{bp}(443)$ can first be corrected for contributions due to a background of nonalgal backscattering particles ($b_{bp}(443)_{NAP}$), which does not covary with phytoplankton. The remaining portion of $b_{bp}(443)$ is then directly related to phytoplankton C by a scaling factor,

$$C = \left(b_{bp}(443) - b_{bp}(443)_{NAP}\right) \times SF \qquad (1)$$

Here, we estimate $b_{bp}(443)_{NAP}$ at 0.00035 m^{-1} by type II regression of monthly mean satellite-retrieved values of $b_{bp}(443)$ and Chl [see *Behrenfeld et al.*, 2005]. The scaling factor (SF = 13000 mg C m^{-2}) is derived such that the resulting C are ~25–40% of total POC as estimated using the same backscatter values [*Loisel et al.*, 2001; *Stramski et al.*, 1999] and average Chl:C values are within the range observed in laboratory studies [*Behrenfeld et al.*, 2005]. Resulting NPP values are surprisingly insensitive to the choice of a specific value for SF. For example, given a range of SF from 10,000 mg C m^{-2} to 20,000 mg C m^{-2} (which causes C/POC ratios to vary from 19% to 60%), annual, global water column NPP varies by <5 Pg C a^{-1}. Thus, at the scale of this analysis, our choice of SF is a second-order problem, though a more detailed error budget is required to determine the largest sources of error in this formulation.

[12] Last, the subsurface C biomass profile below the mixed layer is estimated by evaluating the growth rate at each depth (see section 2.3.2) compared to a constant background rate representing losses, R, assumed to be very small (R = 0.1 d^{-1}). Thus, the C profile is uniform until this threshold is reached, whereupon the C concentration decreases,

$$C(z) = C_{z=0} \qquad \text{if } R \le \mu(z) \qquad (2a)$$

$$C(z) = C_{z=0} \times (\mu(z)/R) \qquad \text{if } \mu(z) < R \qquad (2b)$$

This specification gives a smooth decrease in C at depth and presents C as the net result of growth and loss [*Fennel and Boss*, 2003]. In many ocean regions, profiles of c_p do not show much vertical structure within the euphotic zone, but

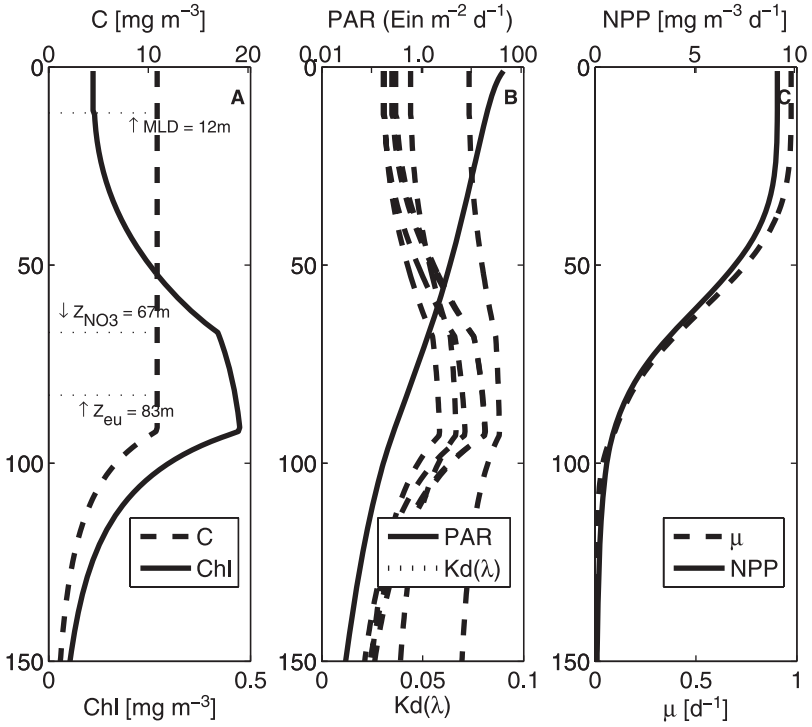

Figure 2. Example profiles from carbon-based productivity model (CbPM) at a single location and time. Data shown are monthly mean values for August in a 1° box in the tropical Pacific (20°N, 110°W). (a) Chl a (mg Chl m^{-3}) and carbon biomass (mg C m^{-3}); also shown are mixed layer depth, nitracline depth, and euphotic depth. (b) Diffuse, spectral attenuation $K_d(\lambda, z)$ (m^{-1}) and photosynthetically available radiation (PAR) (Ein m^{-2} d^{-1}). (c) Phytoplankton growth rate, μ (d^{-1}) and net primary production (NPP) (mg C m^{-3} d^{-1}).

on occasion deep particle maxima can form and will not be captured by our model because this description does not allow for a subsurface maximum (see also section 4). Fortuitously, the exact specification of the C profile does not significantly alter the resulting growth rates or depth-integrated NPP because the changes generally take place deeper in the water column at low-light levels (in fact, using a uniform C profile with depth results in a change of annual global NPP of ~0.5 Pg C a^{-1}, not shown). Thus, given the lack of knowledge about subsurface biomass profiles at the global scale, the description used here is adequate.

2.3. Net Primary Production Model

[13] The NPP model developed here is referred to as the carbon-based production model (CbPM) to reflect the use of b_{bp} data to estimate C as the metric of algal biomass. The CbPM is a depth-resolved, spectral NPP model that iterates through the water column at each global grid point in a manner consistent with the local mixed layer and nitracline depths. Within the mixed layer, properties are constant and equal to the satellite-retrieved values, while below the mixed layer, biological properties are described from a reconstruction of the underwater light field, climatological subsurface nutrient fields and the physiological response to these changes.

2.3.1. Underwater Light Field

[14] Incident, cloud-corrected PAR (Ein m^{-2} d^{-1}) was decomposed spectrally using constant fractions estimated from an atmospheric radiative transfer model [*Ricchiazzi et al.*, 1998]. These fractions are stable within 1–6% depending on wavelength under extremely variable illumination conditions and allow the estimation of spectral irradiance at the surface, $E_d(0^+, \lambda)$. Diffuse attenuation at 490 nm, $K_d(490)$, within the mixed layer was derived from SeaWiFS measurements [*O'Reilly et al.*, 2000], and spectral diffuse attenuation across the visible spectrum, $K_d(\lambda)$, was subsequently calculated using the model of *Austin and Petzold* [1986]. This approach works well on a globally representative data set (NOMAD [*Werdell and Bailey*, 2005]) and was restricted to wavelengths available for validation in the NOMAD data set (412, 443, 490, 510, 555, 665, and 683 nm). On average, 95% of the variability in $K_d(\lambda)$ (range = 84–99%) is accounted for at discrete wavelengths throughout the visible spectrum. Spectral treatment of the light field (both irradiance and attenuation) allows for differential propagation of light with depth to provide an accurate characterization of the underwater light environment.

[15] $K_d(\lambda)$ is assumed to be constant within the mixed layer and then varies below this depth as a function of Chl

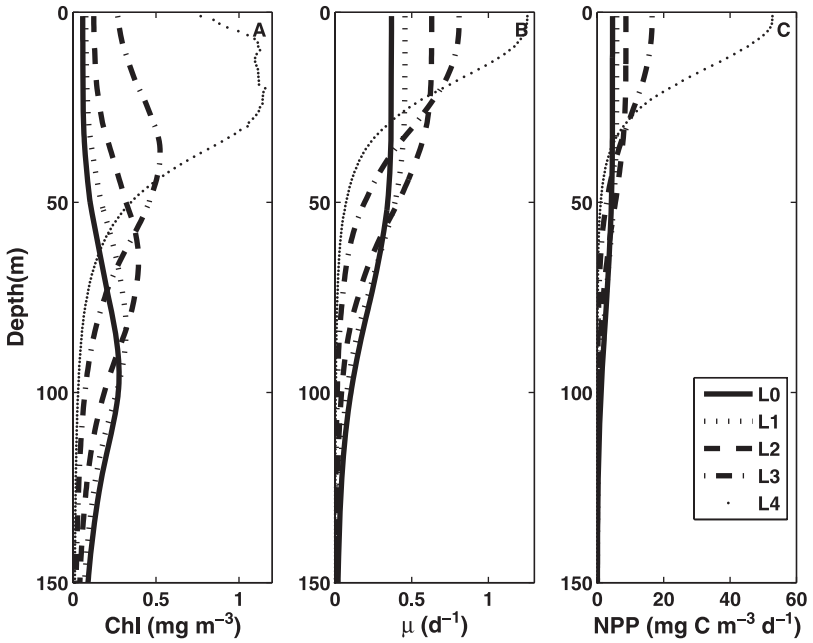

Figure 3. Mean annual profiles in the Northern Hemisphere of Chl, μ, and NPP. Shown for each panel are five curves corresponding to Chl a variance levels L0–L4 (see section 3 for description and also Figure S2). (a) Chl a (mg m^{-3}). (b) Phytoplankton growth rate, μ (d^{-1}). (c) NPP (mg C m^{-3} d^{-1}).

following *Morel and Maritorena* [2001]. As Chl changes with depth (see section 2.3.2), so does the attenuation such that PAR at depth is dependent on the integrated attenuation above it,

$$PAR\ (z) = \int_{400}^{700} E_d(0,\lambda) \cdot e^{-\int_0^z K_d(\lambda)\cdot dz}\, d\lambda \qquad (3)$$

In this way, calculation of the light field proceeds iteratively with depth. We calculate the contribution to attenuation due to components other than Chl (i.e., colored dissolved organic matter (CDOM)) as the difference between the spectrally expanded SeaWiFS estimates and modeled estimates based on surface Chl. This difference is carried through the water column and is equivalent to introducing a uniform profile of CDOM and other attenuating components.

2.3.2. Photoacclimation and Phytoplankton Growth Rates, μ

[16] The primary processes which drive vertical changes in Chl concentration in the CbPM are those associated with physiological, intracellular adjustments to ambient light and nutrient conditions. Photoacclimation, the physiological response to light, was characterized by a decreasing exponential function of light (Figure 1). Specifically, a nonlinear least squares fit to the 99th percentile of the satellite-derived Chl:C distribution as a function of monthly median mixed layer light intensities gives

$$\frac{Chl}{C}_{N-T\max} = \left[0.022 + (0.045 - 0.022)e^{-3\cdot PAR(z)}\right] \qquad (4)$$

[17] This expression represents Chl:C in nutrient-replete, optimal growth conditions, $\frac{Chl}{C}_{N-T\max}$ (i.e., the maximum potential Chl:C for a given irradiance), and the endpoints in equation (4) reflect a low-light maximum in Chl:C and a high-light asymptotic value. In the mixed layer, the acclimation irradiance is taken to be the median PAR in the mixed layer, while below this depth phytoplankton acclimate to the ambient light level. Also shown in Figure 1 is the minimum Chl:C when $\mu = 0$ and is equal to 0.0003 mg Chl (mg C)$^{-1}$. This concept stems from the observation that phytoplankton consistently exhibit positive chlorophyll concentrations when growth has been arrested ($\mu = 0$) [*Geider*, 1987; *Cloern et al.*, 1995]. This no-growth condition was determined by matching the minimum observed satellite Chl:C ($\sim$0.003 mg Chl (mg C)$^{-1}$) with a minimum population growth rate found in the open ocean, $\sim$0.1 d^{-1} [*Jones et al.*, 1996; *Goericke and Welschmeyer*, 1998; *Marañon*, 2005] and extrapolating to $\mu = 0$. It is difficult to compare this value with those reported in literature as the value derived here is for a mixed natural population, whereas laboratory studies represent single species [i.e., *Laws and Bannister*, 1980].

[18] Phytoplankton growth rates, μ (d^{-1}), are calculated in the CbPM from the growth irradiance and Chl:C. In the mixed layer, we assume that Chl:C is vertically uniform and equal to the value estimated from satellite inversion products, Chl and b_{bp}. The corresponding growth irradiance is the median PAR for the mixed layer and represents a well-mixed, photoacclimated community,

$$\mu = \mu_{\max} \quad \frac{\frac{Chl}{C} - \left[\frac{Chl}{C}\right]_{\mu=0}}{\left[\frac{Chl}{C}\right]_{N-T\max} - \left[\frac{Chl}{C}\right]_{\mu=0}} \quad \left[1 - e^{(-5PAR(z))}\right] \qquad (5)$$

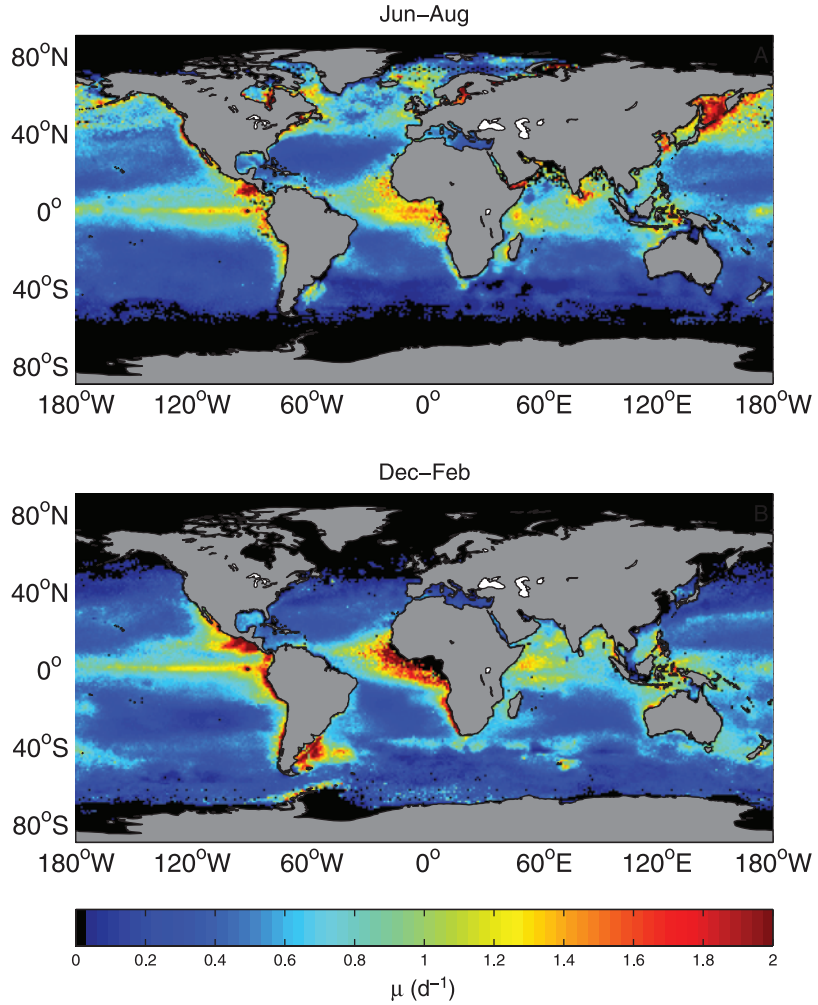

Figure 4. Global maps of mean phytoplankton community growth rates (μ, divisions d^{-1}) in the mixed layer for the boreal summer (top) and winter (bottom). Values are climatological means calculated for 1999–2004.

Here, the first term (μ_{max}) is taken to be 2 d^{-1}, which is roughly the observed maximum growth rate for a natural population [*Banse*, 1991] and sets the upper bound on retrieved μ. The second term in equation (5) describes the combined effects of nutrient limitation and temperature, where satellite Chl:C is scaled relative to a maximum potential Chl:C for that irradiance, $\frac{Chl}{C}_{N-T\max}$, and $\frac{Chl}{C}_{\mu=0}$ is the Chl:C value when $\mu = 0$ (see also Figure 1). The last term describes reductions in growth rate with decreasing light. This decrease in μ at low light occurs because photoacclimation is not sufficient to maintain constant light absorption at all light levels and reflects an optimization based on Chl synthesis and cell division [*Geider*, 1987; *Geider et al.*, 1996]. Further, the strength of light limitation on μ can be characterized by the exponent in equation (5). Laboratory data suggests that its e-folding light level is greater than that which describes the photoacclimation curve for Chl:C (M. J. Behrenfeld, unpublished data, 2007).

[19] Below the mixed layer, calculations of biological quantities are made iteratively with depth. With each incremental increase in depth, the phytoplankton community photoacclimates to a slightly lower light level and changes Chl biomass; this in turn changes spectral attenuation, with which μ and NPP respond accordingly. Below the MLD, the photoacclimation response is similar to the mixed layer (compare equation (4)), but phytoplankton Chl:C is a function of the ambient light level (rather than the median MLD PAR) and can also be affected by a potential relaxation of nutrient stress according to distance from the nitracline,

$$\frac{Chl}{C}(z) = \left[0.022 + (0.045 - 0.022)e^{-3\cdot PAR(z)}\right] - \left[\Delta\frac{Chl}{C}_{NUT}\left(1 - e^{-0.075\Delta z_{NO3}}\right)\right] \quad (6)$$

Here, $\Delta\frac{Chl}{C}_{NUT}$ is a nutrient stress index calculated within the mixed layer as the difference between the satellite-derived Chl:C ratio and the maximum potential Chl:C for that particular growth irradiance, $\frac{Chl}{C}_{N-T\max}$. Global images of

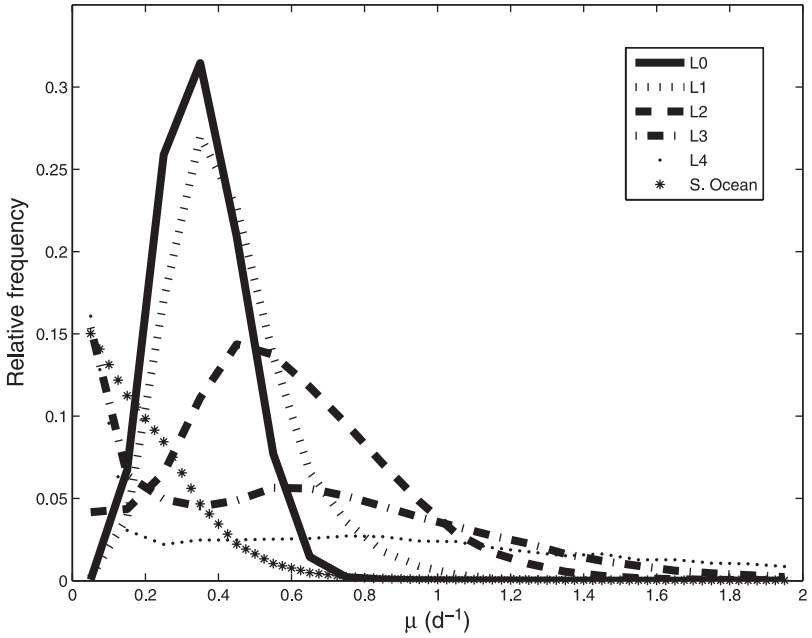

Figure 5. Distribution of climatological monthly mean μ (divisions d^{-1}) for different Chl variance regions (L0–L4) and also Southern Ocean. Values from all 12 months are included, and occurrence is expressed as frequency relative to the total number of instances in each region.

this quantity closely mirror patterns in surface nutrient concentrations and lend further support that the description of photoacclimation given in equation (4) is realistic (Figures S3 and S4). Δz_{NO3} is the distance from the nitracline (valid only at depths shallower than the nitracline and below the MLD). As $\Delta z_{NO3} \rightarrow \infty$, the second term in equation (6) approaches $\Delta \frac{Chl}{C}_{NUT}$, and as $\Delta z_{NO3} \rightarrow 0$, nutrient stress goes to zero. The exponent in the nutrient stress term is equal to 0.075 and gives an e-folding length of ~13 m which serves to approximate a ''fuzzy'' boundary due to diapycnal mixing and diffusion across the nitracline, rather than a sharp jump once the nitracline depth is reached. This scale is likely stratification-dependent, but resulting μ and NPP values are relatively insensitive to changes in this parameter (results not shown). Finally, NPP (mg C m^{-2} d^{-1}) is calculated at each depth,

$$NPP(z) = \mu(z)C(z) \tag{7}$$

[20] In summary, the thickness of the mixed layer compared to the nitracline and light field determines how the model is applied from point to point spatially. Within the mixed layer, all properties (excepting light) are assumed to be homogeneous, and phytoplankton are assumed to be acclimated to a common irradiance; the median PAR. Below the mixed layer, Chl:C and μ are described by equations (4)–(6) and are a function of light and nutrients, depending on the extent of surface nutrient stress and depth of the nitracline. A schematic illustrating the flow of data products representing these quantities and the connectivity between them both within and below the mixed layer is shown in Figure S1.

3. Results: Phytoplankton Growth Rate and Net Primary Productivity

[21] For the results presented here, monthly climatologies for the period 1999–2004 were calculated on a ~1° × 1° spatial grid. An example of CbPM results for a single pixel for the month of August in the tropical Pacific Ocean (20°N, 110°W) is shown in Figure 2. Local MLD, z_{NO3}, and euphotic depth (z_{eu} = 1% surface PAR) are equal to 12 m, 67 m, and 83 m, respectively. These depth horizons give rise to uniform properties through the mixed layer then a subsequent (rapid) increase in Chl from the bottom of the mixed layer to the nitracline that is due to the combined effects of photoacclimation and decreasing nutrient stress. Below the nitracline at ~75 m, there is a more gradual increase in Chl due solely to photoacclimation (Figure 2a). At ~90 m, phytoplankton C begins to decrease as loss processes become greater than growth (μ < R in equation (2)), which in turn causes overall Chl concentration to decrease and gives rise to a subsurface Chl maximum. Changes in Chl are accompanied by corresponding changes in attenuation coefficients ($K_d(\lambda)$) and PAR (Figure 2b). Vertical profiles of μ and NPP are also constant through the mixed layer and then decrease with depth as a function of light and physiological response to the light field (Figure 2c). These profile features can vary substantially in both shape and magnitude as satellite surface quantities, MLD, and z_{NO3} change over space and time.

[22] In order to examine patterns over much broader spatial and temporal scales, oceanic regions can be classified as a

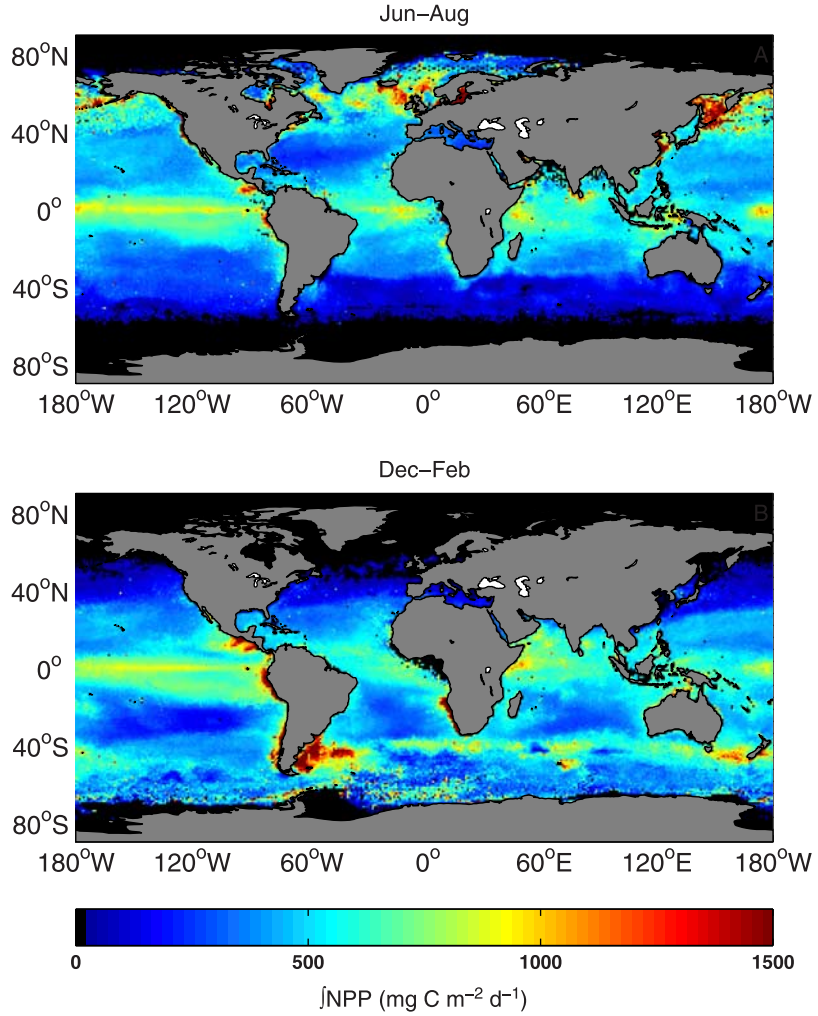

Figure 6. Depth-integrated NPP (mg C m^{-2} d^{-1}) for the boreal summer (top) and winter (bottom). Values are climatological means calculated for 1999–2004.

function of their seasonal variance in Chl [*Doney et al.*, 2003; *Behrenfeld et al.*, 2005]. This classification separates the ocean into functionally different biomes, from oligotrophic to temperate/seasonally productive regions. The standard deviation of annual Chl variability was broken into five variance bins and designated L0 through L4 in increasing order of Chl variance (Figure S2). Average vertical profile properties of Chl(z), μ(z), and NPP(z) differ substantially between these regions and can be compared using annual regional mean values for each property (Figure 3). Surface layer Chl, μ, and NPP decrease monotonically from high-variance regions (L4, e.g., parts of the North Atlantic) to low-variance regions (L0, e.g., North Pacific Subtropical Gyre) while their rate of decay with depth is faster in high-variance regions. Consequently, a larger proportion of water column integrated chlorophyll and primary production is found in the surface layer in high-variance than low-variance regions. Subsurface Chl maxima are progressively deeper and have lower amplitudes in the transition from high- to low-Chl variance regions (~30 m in L3 to ~115 m in L0 regions, Figure 3a), consistent with patterns described by *Morel and Berthon* [1989] (compare their Figure 7). Growth rates are maximal in the surface mixed layer in all variance regions and generally decrease from >1 d^{-1} in L4 areas to <0.5 d^{-1} in L0 regions (Figure 3b). NPP rates also exhibit surface maxima in all Chl variance regions which decay with depth (Figure 3c).

[23] Figure 4 shows the mean μ in the surface mixed layer for both the boreal summer and winter. The modeled seasonal mixed layer μ fields reflect patterns resulting from light and nutrient limitation, as well as community composition (not captured in our model, but can contribute significantly to Chl:C variability). Values range from near zero to almost two divisions d^{-1}, though only a small percentage of μ values (<1%) exceed 1.5 d^{-1}. Highest values are generally found along eastern boundary and equatorial upwelling regions. Elevated μ values in the latter, however, are likely overestimates by ~15–20% due to the unique effect of iron limitation on chlorophyll synthesis in HNLC regions resulting in a reduction in μ that is not reflected in the Chl:C ratio [*Behrenfeld et al.*, 2006]. Oligotrophic gyres exhibit lower growth rates, but there is

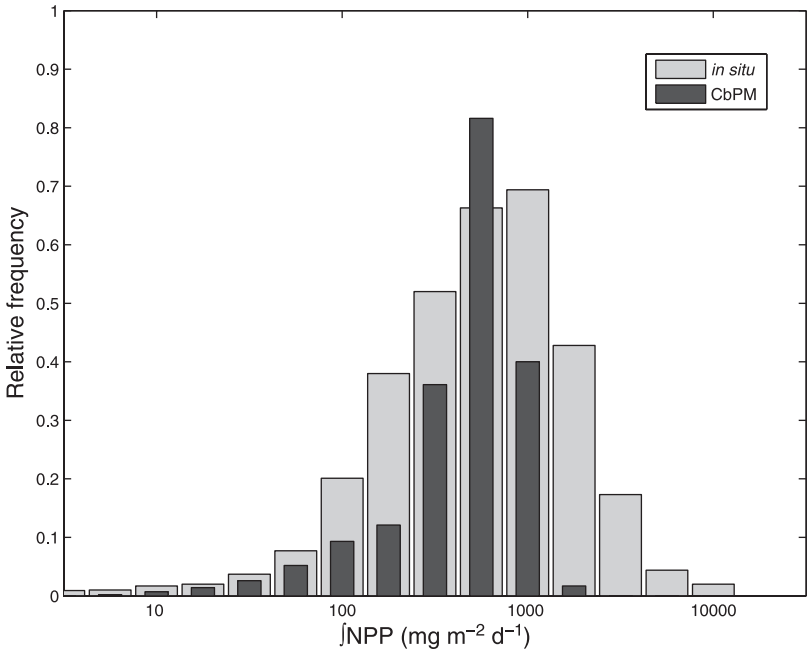

Figure 7. Histogram of depth-integrated NPP values ($\int$NPP). Light gray represents ^{14}C measurements compiled by *Behrenfeld and Falkowski* [1997]. Dark gray represents CbPM results sampled at same locations and same climatological months. N = 3043.

significant heterogeneity within and between these regions (compare summertime North Pacific with wintertime North Atlantic). Extreme seasonality in μ is observed at very high latitudes and is associated with strong seasonal variations in mixing depths and light availability. Accordingly, very low μ values (<0.3 d^{-1}) extend zonally above ~40°N and below ~40°S in each hemisphere's winter. Even in the austral summer when Southern Ocean Chl levels are high, average growth rates there are surprisingly low (~0.28 d^{-1}) and are likely the result of perennially deeper mixed layers and iron limitation [*de Baar and Boyd*, 1999; *Boyd et al.*, 2000].

[24] Frequency distributions of monthly mean growth rates throughout the year (all 12 months combined) for different Chl variance regions are shown in Figure 5. The global annual median μ for the whole ocean is ~0.43 d^{-1}, but within each individual region average values may differ significantly. The cumulative distribution function (not shown) indicates that ~52% of the annual mean growth rates are <0.5 d^{-1}, while nearly 94% are less than 1 d^{-1}. Low-variance environments (those classified as L0 + L1) have annual mean μ equal to 0.39 ± 0.13 d^{-1}, and the enormous areal extent of these oligotrophic waters undoubtedly influences the global median μ value. However, wintertime contributions from high-latitude light-limited regions, particularly the Southern Ocean which comprises ~73% of μ < 0.3 d^{-1}, also add to the prominence of low growth rates. The bimodal character of the L3 μ distribution (peaks at ~0.05 and 0.6 d^{-1}) reflects the seasonal cycle of deep mixing and subsequent spring/fall blooms (e.g., North Atlantic). Growth rate estimates in each of these regions are broadly consistent with those reported in the literature [*Marañon*, 2005; *Jones et al.*, 1996; *Goericke and Welschmeyer*, 1998; *Boyd et al.*, 2000]. *Marañon* [2005] synthesized growth rate measurements for the Atlantic subtropical gyres (spanning L0 and L1) and reported values between 0.13 and 0.62 d^{-1} depending on hemisphere and time of year. *Jones et al.* [1996] found slightly higher values for the subtropical north Pacific gyre (0.7 d^{-1}). In the Southern Ocean, μ measurements made before and during iron enrichment experiments have shown that background growth rates are extremely low (<0.15 d^{-1}) and upon enrichment do increase, but are still low (0.3–0.4 d^{-1}) [*Boyd et al.*, 2000].

[25] Global fields of summer and winter depth-integrated NPP ($\int$NPP) from the CbPM are shown in Figure 6. Maximum $\int$NPP values are ~1500 mg C m^{-2} d^{-1} and confined to productive upwelling regions such as Peru, the Benguela Current system, the Gulf of Tehuantepec, and Costa Rica Dome. Sustained values near 500 mg C m^{-2} d^{-1} are found throughout much of the tropical ocean, except for the central oligotrophic gyres. In some cases, small-scale heterogeneity in $\int$NPP can be traced to artifacts in mixed layer depth products (in the Southern Ocean for example). To illustrate the overall distribution of $\int$NPP values, a representative global sampling is drawn to best match an extensive collection of field data previously presented by *Behrenfeld and Falkowski* [1997] (Figure 7). Monthly $\int$NPP from the CbPM were calculated at the same locations and for the same climatological months as in situ ^{14}C measurements which are from a historical database (1958–1994). The distributions and overall correspondence match well (Figure 7). The CbPM underestimates extremely high values seen in the measurements, but this is to be expected since these records are largely from coastal

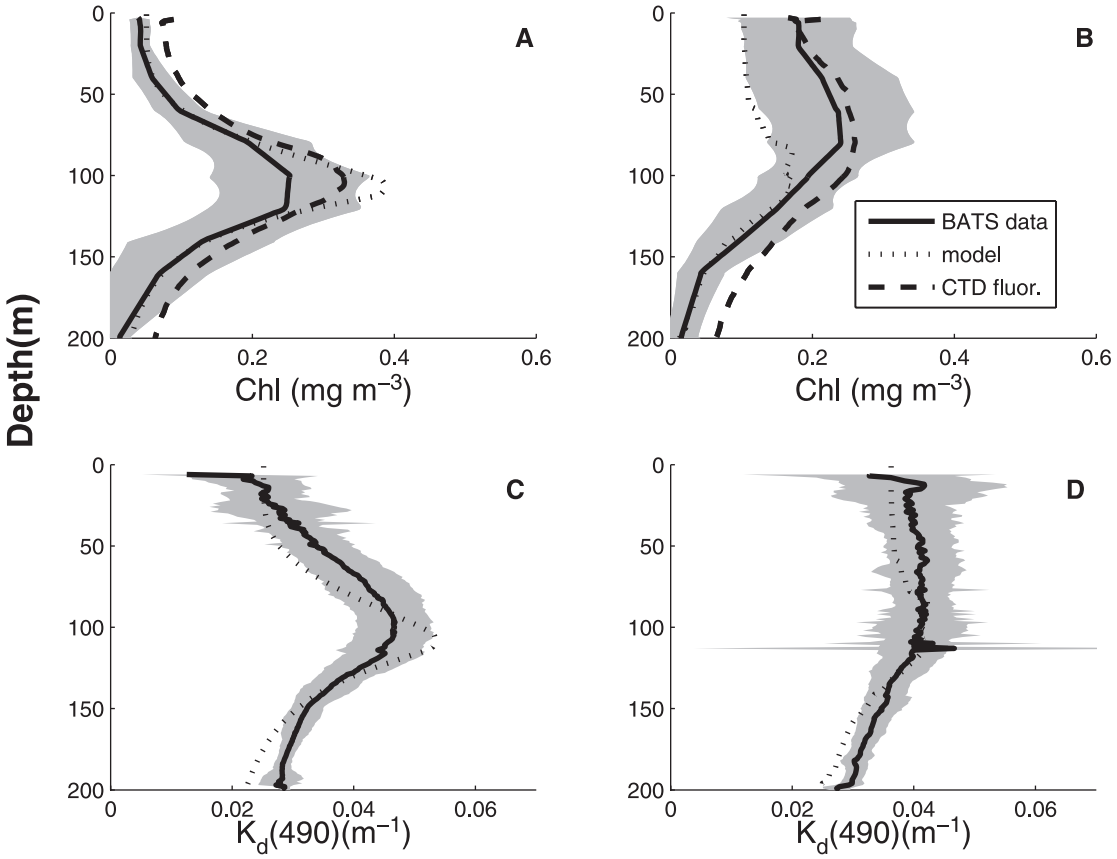

Figure 8. Mean Chl and $K_d(490)$ profiles for summer (June–August) and winter (December–February) at the Bermuda Atlantic Time-series Study (BATS) site. Solid curves are mean values from measurements ($\pm 1\sigma$ in the gray-shaded area); dotted curves are mean values for the same time period from the CbPM. Also shown are mean relative fluorescence profiles from CTD-mounted fluorometer for same time periods (dashed curves). (a) Summer Chl (mg m^{-3}). (b) Winter Chl (mg m^{-3}). (c) Summer $K_d(490)$ (m^{-1}). (d) Winter $K_d(490)$ (m^{-1}).

locations, and in addition the CbPM results are average monthly values.

4. Discussion

4.1. Comparison With Field Measurements

4.1.1. Vertical Comparison

[26] The CbPM has a variety of diagnostic products that can be independently validated with in situ data. The processes which we seek to describe are to first order, directly dependent on the quantity and quality of light available to the phytoplankton community, and thus, an accurate characterization of the underwater light field is critical. As an initial evaluation of our spectral reconstruction and vertical propagation of light through the water column, we compare model descriptions to field data collected as part of BATS and the Bermuda Bio-Optics Project (BBOP) [*Siegel et al.*, 2001; *Steinberg et al.*, 2001]. Figure 8 shows mean profiles of Chl and $K_d(490)$ at the BATS site during the boreal summer and winter months (from 1997–2004). Also shown are the climatological mean profiles from the CbPM during the same seasons at the BATS/BBOP sampling site. Correspondence between measured and modeled properties is remarkable considering the extremely different natures of the estimates, with the modeled values being fairly coarse spatial and temporal estimates based on satellite-retrieved information and climatological MLD and nitracline depths. Specifically, the differences between measured and modeled Chl profiles fall within the 1 standard deviation (1σ) envelope of the measurements at nearly all depths (gray-shaded areas in Figures 8a and 8b). The summer Chl profile shows a distinct deep chlorophyll maximum near 100 m near the bottom of the euphotic zone. This feature is also reproduced in the mean CbPM Chl profile at nearly the same depth (Figure 8a). Mean CTD-mounted fluorometer profiles (unscaled) for the same seasonally averaged time periods also compare well to the modeled Chl profile ($r^2 = 0.97$ and 0.80 for summer and winter).

[27] Winter Chl values are elevated throughout the upper 100 m with a large degree of variability at these depths compared to summer profiles (Figure 8b). Notably, variability in measured properties themselves is extremely large during winter months because of drastic changes in mixing

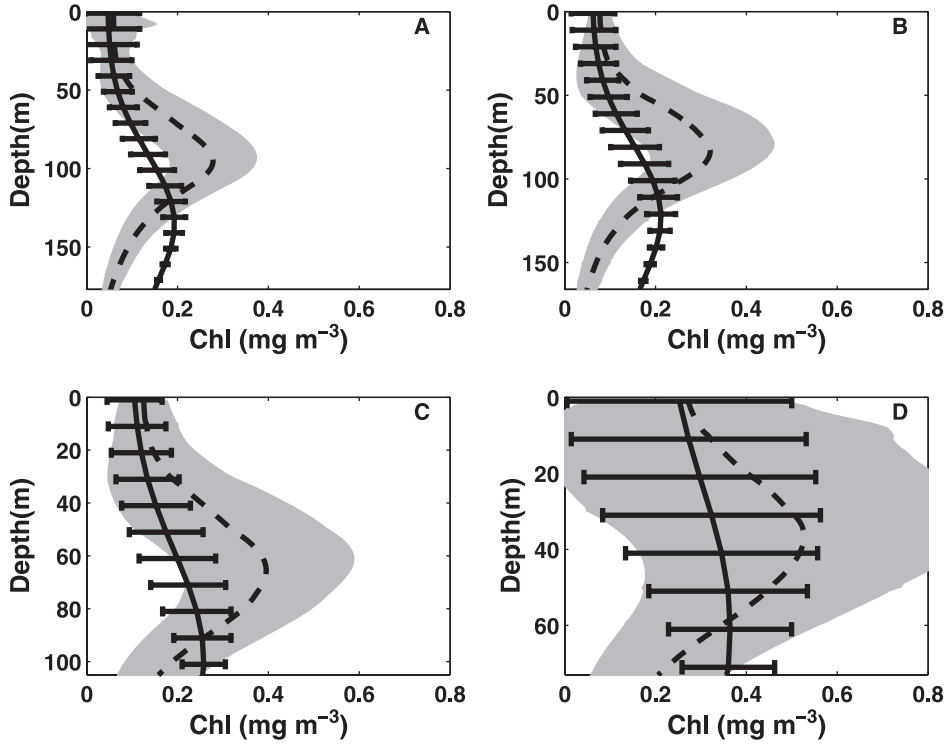

Figure 9. Comparison of modeled Chl(z) profiles from CbPM and *Morel and Berthon* [1989]. In all panels, dashed curve and gray-shaded area are mean ($\pm 1\sigma$) Chl profiles averaged over a specific Chl variance bin, and solid curve and error bars are mean ($\pm 1\sigma$) Chl profiles predicted by *Morel and Berthon* [1989] over same area. (a) L0. (b) L1. (c) L2. (d) L3. Limits of the *y* axes correspond to 1.5x mean euphotic depth, the range over which the Morel and Berthon predictions are valid.

depth (σ_{MLD} = 38 m), making the mean profile less representative of any particular Chl profile. There is also a clear offset between the mean model and measured Chl concentration within the mixed layer that is traceable to the satellite retrievals of Chl and not the CbPM. Some of the mismatch between measured and modeled Chl can be attributed to CDOM absorption and its vertical variability [*Siegel and Michaels*, 1996; *Nelson et al.*, 1998], but is also due to the small dynamic range of Chl a observed at the BATS site.

[28] Mean model and field determinations of $K_d(490)$ for the summer and winter periods are shown in Figures 8c–8d, and again, correspondence is very good (normalized RMSE = 12% and 7% for summer and winter profiles, respectively). $K_d(490)$ profiles generally exhibit patterns similar to that in Chl profiles, having a pronounced subsurface maximum near the base of the euphotic zone in the summer and elevated, uniform values in the winter. During the summer, the CbPM underestimates $K_d(490)$ between ~20–90 m, the depth region associated with CDOM production, which possibly accounts for this offset. Wintertime surface layer modeled and measured $K_d(490)$ values agree better than Chl profiles, indicating good correspondence between satellite and in situ radiances and again pointing to inaccuracies in treatment of CDOM as an important factor in discrepancies between retrieved Chl values and field measurements.

[29] A widely used approach for reconstructing subsurface variability in Chl is the method of *Morel and Berthon* [1989] (hereafter MB89). Here, we applied the method of MB89 to monthly climatological surface Chl fields in order to compare average Chl(z) profiles to those predicted by the CbPM. Figure 9 shows the mean and standard deviation envelopes of Chl(z) from the two approaches averaged over Chl variance bins L0–L3 (L4 not shown). In all cases, the CbPM predicts a higher subsurface maximum and also places the peak shallower in the water column, especially in the more oligotrophic examples (L0 and L1, Figures 9a–9b). These discrepancies might be due to several things. The MB89 profiles do not allow for the complete decay of the subsurface maxima and further, the profile prediction is done in terms of depth relative to the euphotic depth (=1% surface PAR). Since euphotic depths estimated by MB89 are always shallower than those predicted by the CbPM (not shown), this acts to deepen the peak of the Chl maximum in terms of geometric depth. In the more productive waters (L2 and L3) the ranges of variability indicated by the standard deviations generally overlap, but are rather large (Figures 9c–9d). MB89 predicts a much more constant profile, while on average the CbPM Chl profile still shows an increase of ~75% from the surface to the peak at ~40 m. The locations that comprise L2 and L3 areas are generally temperate, seasonal environments that exhibit strong seasonal variation in mixing and phytoplankton biomass, hence the large

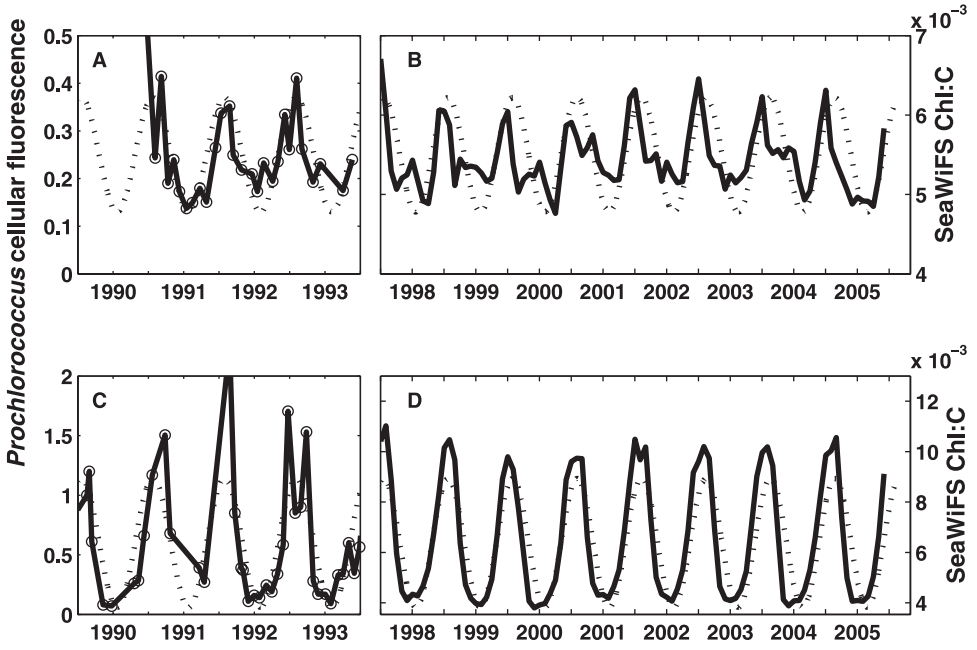

Figure 10. Monthly time series of Chl:C at the Hawaii Ocean Time-series (HOT) and BATS sites. (a) *Prochlorococcus* cellular fluorescence at HOT (reproduced with permission from *Winn et al.* [1995]). (b) Average Chl:C estimated by Sea-Viewing Wide Field-of-View Sensor (SeaWiFS) in the Chl variance bin containing HOT site. In both Figures 10a and 10b, modeled seasonal signal (dotted curve) from *Winn et al.* [1995] is also shown. (c) *Prochlorococcus* cellular fluorescence at BATS [from *Durand et al.*, 2001]. (d) Average Chl:C in the Chl variance bin containing BATS site estimated by SeaWiFS. In both Figures 10c and 10d the modeled seasonal fit (dotted curve) to *Durand et al.* [2001] is also shown.

standard deviations associated with the Chl profiles in these areas. While deep mixing occurs regularly, we expect to see some subsurface maximum due to photoacclimation as it occurs on timescales of the order of a generation time.

4.1.2. Temporal Comparison

[30] Photoacclimation is the physiological adjustment to a changing light environment and is primarily manifest as a change in cellular Chl content that occurs over many timescales. At the seasonal scale, we might expect phytoplankton to have decreased cellular Chl during the summer and increased cellular Chl in the winter due to differences in insolation and mixing depths. *Winn et al.* [1995] demonstrated this pattern in the North Pacific Gyre at the Hawaii Ocean Time-series (HOT) site, which is representative of a large portion of global oligotrophic waters. Using flow cytometry, the authors found that seasonal surface patterns in cellular fluorescence of *Prochlorococcus* were consistent with photoacclimation and exhibited a wintertime maximum and summertime minimum. Further, the pattern was consistent from year to year and well described by a simple sinusoidal function. Figures 10a–10b show the data reported by *Winn et al.* [1995] in addition to monthly satellite Chl:C estimates in the Chl variance bin surrounding the HOT site (Figure 10b). While the absolute values (and units) for these two time series differ because one is a fluorescence measurement of *Prochlorococcus* and the other a satellite Chl:C ratio of the entire phytoplankton population, the periodicity of the seasonal cycle is nearly identical. Similar measurements of *Prochlorococcus* cellular fluorescence have been reported for the BATS site and interpreted as photoacclimation as well [*Durand et al.*, 2001]. The seasonal cycle at BATS is similar to that at HOT with summer minima and winter maxima, and the corresponding satellite Chl:C values for this site also exhibit the same pattern (Figures 10c–10d). What this shows is that in these oligotrophic waters, where seasonal variation in Chl:C is driven primarily by photoacclimation, satellite estimates of Chl:C also capture the photoacclimation signal.

[31] The HOT and BATS data records also provide long-term, methodologically consistent ^{14}C NPP measurements to compare with the model NPP estimates. Figure 11 shows time series of depth-integrated (Figure 11a) and depth-specific (Figures 11b–11c) primary production at the HOT site. Seasonal variability is not very large in water column integrated NPP ($\int$NPP) and has a peak-to-peak magnitude of $\sim$300 mg C m^{-2} d^{-1} with maxima in the late spring. Also shown in Figure 11a are model estimates for depth-integrated primary production from the vertically generalized production model (VGPM) of *Behrenfeld and Falkowski* [1997] and the CbPM. While the VGPM captures the seasonality seen in the HOT record, there is a large, systematic bias (normalized mean bias (NMB) = −40%) (Table 1). In contrast, the estimates from the CbPM capture the mean value much better (NMB = 13%), but do not show the seasonal variation (coefficient of variation (CV) = 0.09) (Table 1). This mismatch between CbPM and field results is

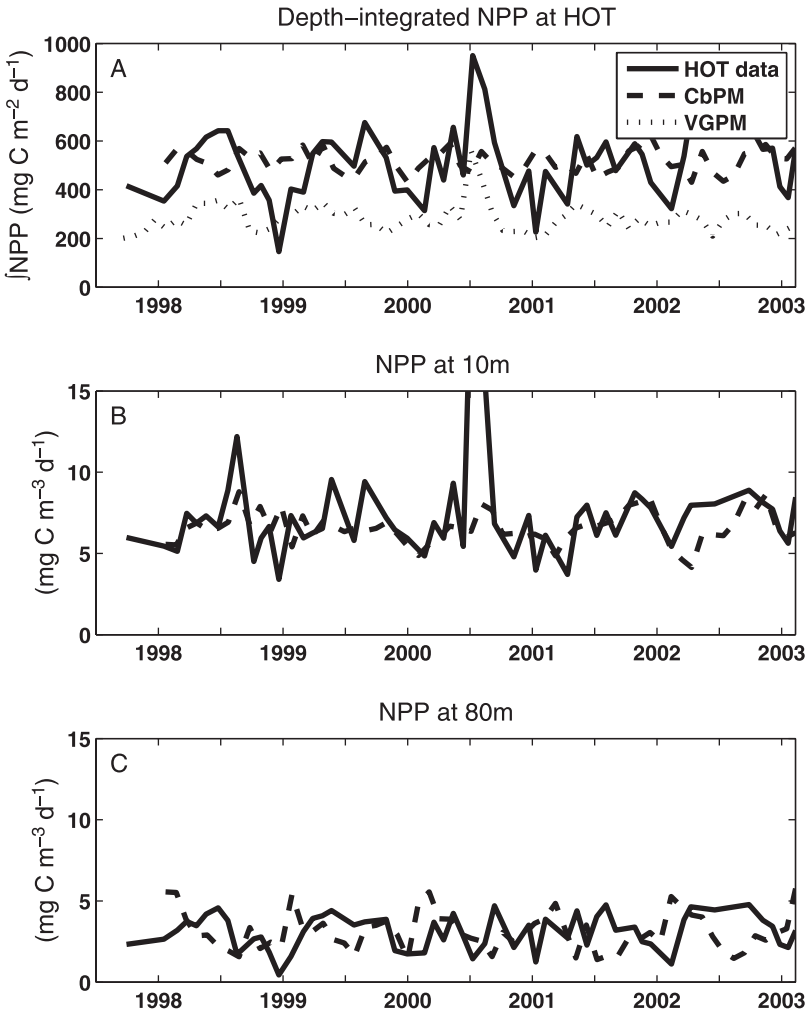

Figure 11. Time series of NPP at HOT site. (a) Water column integrated NPP (mg C m^{-2} d^{-1}) from ^{14}C incubations (solid curve), CbPM (dashed curve), and vertically generalized production model (VGPM) (dotted curve). (b) Depth-specific NPP (mg C m^{-3} d^{-1}) at 10 m. (c) Depth-specific NPP (mg C m^{-3} d^{-1}) at 80 m.

not seen so much in estimates of surface primary production (Figure 11b, NMB = 1%, r = 0.34 at 10 m), but rather can be traced to discrepancies at depth (Figure 11c) (r = 0.13 at 80 m). Since increases in Chl and Chl:C with depth in the CbPM are due largely to photoacclimation, this suggests that the seasonal pattern observed in the HOT record is due instead to accumulation of phytoplankton biomass and production at depth. This is consistent with findings at this site which show that changes in phytoplankton productivity at depth can be attributed to accumulation of phytoplankton biomass rather than photoacclimation [*Winn et al.*, 1995; *Letelier et al.*, 1993].

[32] Comparison to the BATS ^{14}C record highlights some interesting aspects of both the CbPM and the annual cycle at BATS. Seasonal differences in $\int$NPP are larger than at HOT, although the mean values are nearly the same ($\sim$500 mg C m^{-2} d^{-1}). A time series of surface NPP shows recurrent springtime maxima in the ^{14}C record which are not reproduced in the CbPM NPP estimates. This is partly because monthly satellite Chl retrievals underestimate the actual Chl values during this period by $\sim$120% (range = 30–230%) (not shown). If the CbPM is run using in situ BATS Chl values, the spring bloom events appear in the resulting surface NPP estimates and correspond well with the field measurements in both timing and magnitude (Figure 12b). However, there are still instances where maxima in ^{14}C NPP measurements are not well captured by the model and in fact, show minima in estimated surface NPP (e.g., 1998 and 2002). In these cases, much of the bloom actually occurs while winter mixing is still rather deep, greatly lowering acclimation irradiances in the model and consequently, the predicted growth rates. This emphasizes the distinction between physical mixing depth and a "physiological mixing depth", the latter often being shallower. The physiological response to mixing has to be a time-averaged phenomenon over the timescale of photoacclimation ($\sim$hours to days). Thus, the recent history (<1 month) of vertical mixing near the onset of the spring bloom can act to decouple mixing

Table 1. Summary Statistics for NPP Measurements and Model Predictions at HOT and BATS[a]

	Mean, mg C m^{-2}	Std, mg C m^{-2}	CV	NMB,[b] %	r
		HOT			
Data	497	141	0.28	-	-
VGPM	275	54	0.2	−40 ± 22	0.53
CbPM new	514	48	0.09	13 ± 44	0.04
Data, 10 m	6.8	1.6	0.24	-	-
CbPM new, 10 m	6.5	1	0.15	1 ± 25	0.34
		BATS			
Data	457	158	0.35	-	-
VGPM	328	166	0.51	−20 ± 41	0.29
CbPM new	287	81	0.28	−29 ± 37	0.32
CbPM new, tuned	390	245	0.65	−18 ± 56	0.02

[a]"CbPM 2005" refers to the carbon-based productivity model presented by *Behrenfeld et al.* [2005], while "CbPM new" is the approach described in this work. VGPM refers to *Behrenfeld and Falkowski*'s [1997] vertically generalized production model. CV is the coefficient of variation, and NMB is the normalized mean bias. NPP is net primary production. "Tuning" the CbPM at the Bermuda Atlantic Time-series Study (BATS) site consisted of using in situ Chl measurements. N = 75 for Hawaii Ocean Time-series (HOT), and N = 72 for BATS.

[b]NMB = (model − data)/data × 100.

scales and phytoplankton physiological response in the model and in the field. At depth (80 m) another interesting pattern is observed in field data where elevated production appears in early summer and remains until fall. It is possible that this production is a response to episodic nutrient inputs [*McGillicuddy and Robinson*, 1997; *Siegel et al.*, 1999] or phytoplankton biomass accumulation at depth as observed at HOT. The latter suggestion is plausible because *Prochlorococcus* generally bloom at depth during the summer/fall in the Sargasso Sea and comprise ∼25–50% of phytoplankton C during these times [*Durand et al.*, 2001].

4.2. Comparison With Other Global NPP Estimates

[33] It is instructive to put the annual NPP estimates generated here in context of similar results reported elsewhere. The CbPM estimate of 52 Pg C a^{-1} for global annual ocean NPP is similar to previously published values based on satellite Chl (Table 2). Limiting our discussion to recent estimates, we find the range of values to span a factor of ∼1.5, from 44 to 67 Pg C a^{-1} (see Table 2 for references). *Carr et al.* [2006] also showed that the range was nearly a factor of 2 across very different approaches, i.e., global circulation models, bio-optical models, and empirical models. Much of this variability can be attributed to the source of input information. For example, one of the higher estimates comes from *Behrenfeld et al.* [2005] where euphotic depths (z_{eu}) and growth irradiance were estimated from $K_d(490)$ and thus, overestimated. Applying a simple Chl-dependent parameterization for z_{eu} [*Morel and Maritorena*, 2001] to this same model yields a more conservative estimate of 35 Pg C a^{-1} rather than 67 Pg C a^{-1}. *Behrenfeld and Falkowski* [1997] showed that by changing the function describing the physiology in their model to match that of *Antoine and Morel* [1996], the global annual totals from the two models were nearly the same. Thus, when input fields are standardized and bio-optical and photophysiological assumptions are reconciled, the range in global annual ∫NPP becomes much narrower.

[34] While the CbPM gives a global annual ocean ∫NPP estimate similar to other models, it deviates significantly with respect to the distribution and timing of production. Conventional "chlorophyll-based" models assign all changes in Chl to a change in biomass, which then translates directly to NPP. The CbPM, however, distinguishes between changes in Chl due to physiology and to growth and treats each accordingly. This distinction, although well known from laboratory-based investigations, has been universally ignored in remote sensing estimates of Chl and NPP. Comparing the CbPM and VGPM estimates of NPP for broad functional regimes (Table 3) shows higher open ocean gyre values of ∼11 Pg C a^{-1} or ∼21% of the total for the CbPM, than the VGPM (5 Pg C a^{-1} or ∼11% of total). The largest difference between the models is at high latitudes, with 13 Pg C a^{-1} (25% of the total) and 19 Pg C a^{-1} (42% of the total) for the CbPM and VGPM, respectively. If the CbPM results are further compared with those of *Behrenfeld et al.* [2005], we find that although the annual totals were significantly different (67 Pg C a^{-1} compared to 52 Pg C a^{-1}), the broad spatial patterns remain similar with respect to the VGPM (Table 3). This suggests that even though the details of the subsurface light field and parameterization of photoacclimation affect the magnitude of NPP, the resultant patterns arise from spatial variations in phytoplankton physiology as seen in Chl:C.

4.3. Model Considerations and Future Directions

[35] The CbPM described here is a fully developed version of the idea first put forth by *Behrenfeld et al.* [2005]. Significant improvements include wavelength and depth resolution which yield detailed profile information on Chl, μ, and NPP, a more robust derivation of the photoacclimation model, and an accounting for variable nutrient stress in the vertical. Nevertheless, a variety of model components require further refinements and validation. For example, the CbPM employs a scattering (b_{bp}) to C relationship that relies partially on the relatively invariant nature of the particle size spectrum. Fortunately, this assumption holds over much of the ocean [*Stramski and Kiefer*, 1991; *Stramski et al.*, 2004], but there are obvious examples when this may become invalid [*Loisel et al.*, 2006]. Large diatom or coccolithophorid blooms, for example, can significantly alter the slope of the particle size distribution. *Balch et al.* [2005] suggest that coccolithophorids are much more widespread than previously thought and their calcium carbonate exoskeletons (and detached coccoliths) have a disproportionately large contribution to backscattering [*Balch et al.*, 1989, 1999]. Additionally, these organisms synthesize organic carbon through photosynthesis and particulate inorganic carbon (PIC) into their calcareous plates, further confounding a single relationship between b_{bp} and C. Proper characterization of the relationship between b_{bp} and C for these organisms will require the separation of scattering due to PIC and from phytoplankton organic C. Remote assessment of taxon-specific groups such as those proposed by *Balch et al.* [2005] or *Alvain et al.* [2005] might be used to classify ocean areas in terms of dominant phytoplankton

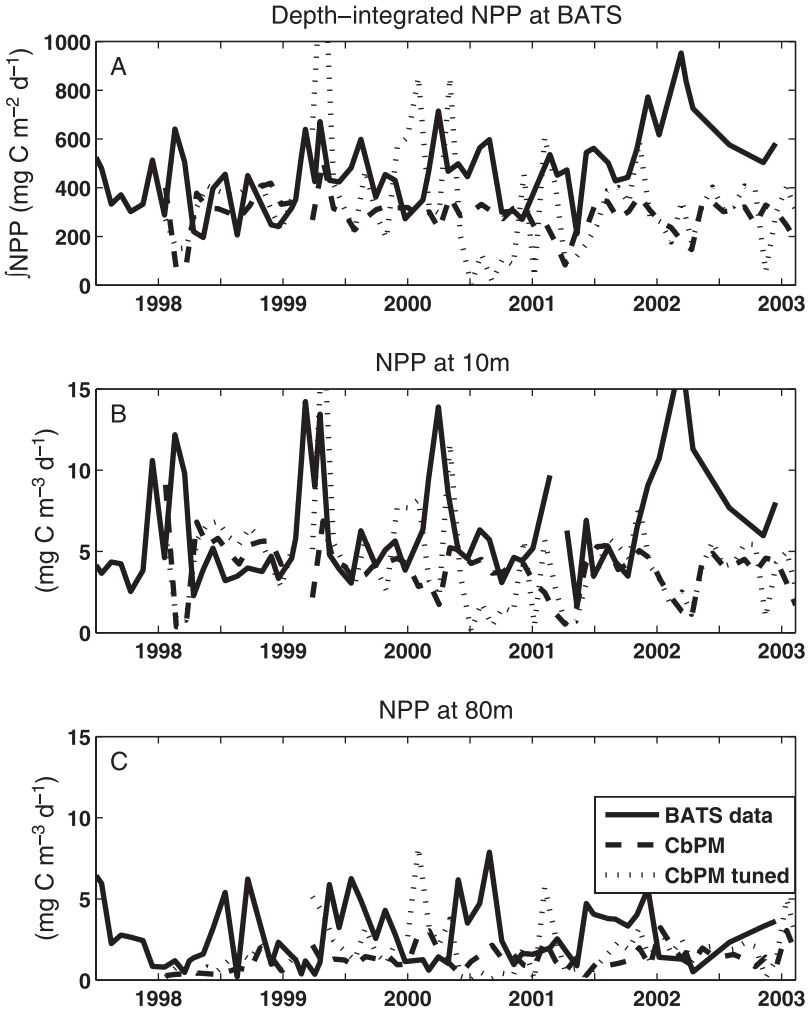

Figure 12. Time series of NPP at BATS site. (a) Water column integrated NPP (mg C m^{-2} d^{-1}) from ^{14}C incubations (solid curve), CbPM (dashed curve), and CbPM run using in situ measured Chl from BATS (dotted curve). (b) Depth-specific NPP (mg C m^{-3} d^{-1}) at 10 m. (c) Depth-specific NPP (mg C m^{-3} d^{-1}) at 80 m.

groups and apply specific b_{bp} to C conversions. In addition, an approach such as that described by *Loisel et al.* [2006] might be used to scale the b_{bp} retrievals accordingly and thus the resulting C.

[36] The improved physiology incorporated by the CbPM over earlier models is still a simplified description of a natural phytoplankton population. Photoacclimation for mixed natural populations is not well studied and nearly all relevant laboratory and field studies are for single species. Nevertheless, from these studies we might expect that the low-light maximum in Chl:C should increase with increasing temperature [*Geider*, 1987; *Cloern et al.*, 1995] and the light-saturated minimum should decrease with increased nutrient stress [*Laws and Bannister*, 1980; *Geider et al.*, 1998]. Thus, the nature of the Chl:C versus light relationship should change depending upon environmental conditions. Additionally, we are unable to account for species-specific variability in Chl:C. It is unclear how this will manifest itself in mixed phytoplankton populations, but it is widely known that Chl:C and its response to light and nutrients varies from species to species [*Geider*, 1987; *MacIntyre et al.*, 2002]. Again, novel remote sensing approaches to obtain phytoplankton functional groups from

Table 2. Mean Annual Global NPP Estimated From Various Model Sources[a]

	∫NPP, Pg C a^{-1}	Description
This model (CbPM)	52	C-based, spectral
VGPM	44	Chl-based, DIM
Behrenfeld et al. [2005]	67	C-based, DIM
Antoine and Morel [1996]	46	Chl-based, WRM
Longhurst et al. [1995]	50	Chl-based
Moore et al. [2001]	48	GCM
Carr et al. [2006]	51	mean of 31 global models

[a] ∫NPP is depth-integrated NPP. DIM is depth-integrated model; WRM is wavelength resolved model; GCM is global circulation model. See *Carr et al.* [2006] for summary of several other models.

Table 3. Annual, Areally Integrated NPP for Various Regions of the Global Ocean[a]

$\int$NPP, Pg C a^{-1}	VGPM	*Behrenfeld et al.* [2005]	CbPM, this work
Annual	45	67	52
Gyres	5 (11%)	20 (29%)	11 (21%)
High latitudes	19 (42%)	11 (17%)	13 (25%)
Subtropics	18 (40%)	33 (49%)	25 (48%)
Southern Ocean, $\theta < -50°$S	2 (4%)	3 (4%)	2 (4%)

[a]Results shown are for CbPM, *Behrenfeld and Falkowski*'s [1997] VGPM, and *Behrenfeld et al.*'s [2005] initial carbon-based model. Values in parentheses indicate percentage of annual total in each region. Regions defined by seasonal Chl variance as described in text (L0 + L1 = Oligotrophic, L2 = Subtropical, and L3 + L4 = High Latitude).

space [e.g., *Alvain et al.*, 2005] may help constrain this variability in the future. Another aspect of photoacclimation which could be further explored is acclimation to total absorbed radiation rather than total available radiation. It is reasonable to believe that changes in intracellular Chl content are cued by the amount of intercepted photons rather than available ones and thus, could be better described as such.

[37] Finally, the requirement for subsurface information such as MLD and nitracline depths (z_{NO3}) on the global scale also presents a challenge. Reliance on numerical model output and historical climatologies constrain the spatial and temporal output resolution and potentially affect CbPM results. For example, MLD is negatively correlated with NPP as deeper mixing results in phytoplankton acclimation to lower irradiances and thus lower growth rates in the mixed layer. *Carr et al.* [2006] examined model NPP sensitivity to changes in MLD for a small set of stations (N = 11) and found resultant NPP estimates to vary by a factor of 2 over a wide range of MLD perturbations. Accurate estimates of MLD and MLD light climate are critical for many research purposes and should be an important future research effort in either remote sensing or numerical models.

[38] It is important to point out that many of the caveats just mentioned are common to all NPP modeling, not just the CbPM. For example, many Chl-based models do not include MLD explicitly, but contain mixed layer information through photoacclimation effects on retrieved Chl values. Another common problem encountered is the effect of species composition on Chl and physiological terms, an aspect which satellites cannot currently address. Last, conversion of Chl, when used as an indication of biomass, to a rate of carbon fixation implies a fixed Chl:C ratio. These confounding aspects require a more thorough error budget and sensitivity study to evaluate the effects on CbPM performance.

5. Summary

[39] We have demonstrated a means to estimate NPP from satellite-derived information that is fundamentally different from previous approaches. This new C-based approach allows for the separation of biomass and physiological changes in Chl. Without considering both of these influences, standard Chl-based NPP models will provide an incorrect picture of phytoplankton production, as much of the surface ocean is dominated by physiological changes in Chl. Interestingly, when we apply our approach to global satellite data, the annual depth-integrated primary production ($\sim$52 Pg C a^{-1}) is similar to Chl-based estimates. However, upon further inspection of the resulting NPP distribution, we find that the spatial nature and timing of the NPP is significantly different in all ocean basins [*Behrenfeld et al.*, 2005]. This result will have implications for estimated export of fixed C out of the surface ocean and must be considered in future work. It is our hope that the current contribution will highlight some of the problems in current satellite NPP modeling (i.e., capturing physiologic variability) and provide a better alternative as acclimation to light and nutrients can be addressed.

References

Alvain, S., C. Moulin, Y. Dandonneau, and F. M. Breon (2005), Remote sensing of phytoplankton groups in case 1 waters from global SeaWiFS imagery, *Deep Sea Res., Part I*, *52*, 1989–2004, doi:10.1016/j.dsr.2005.06.015.

Antoine, D., and A. Morel (1996), Oceanic primary production, 1, Adaptation of a spectral light-photosynthesis model in view of application to satellite chlorophyll observations, *Global Biogeochem. Cycles*, *10*, 43–55, doi:10.1029/95GB02831.

Austin, R. W., and T. J. Petzold (1986), Spectral dependence of the diffuse attenuation coefficient of light in ocean waters, *Opt. Eng.*, *25*, 473–479.

Babin, M., A. Morel, V. Fournier-Sicre, F. Fell, and D. Stramski (2003), Light scattering properties of marine particles in coastal and open ocean waters as related to the particle mass concentration, *Limnol. Oceanogr.*, *48*, 843–859.

Balch, W. M., M. Abbott, R. W. Eppley, and F. M. H. Reid (1989), Bias in satellite derived pigment measurements due to coccolithophorids and dinoflagellates, *J. Plankton Res.*, *11*, 575–581, doi:10.1093/plankt/11.3.575.

Balch, W. M., D. T. Drapeau, T. L. Cucci, R. D. Vaillancourt, K. A. Kilpatrick, and J. J. Fritz (1999), Optical backscattering by calcifying algae – Separating the contribution by particulate inorganic and organic carbon fractions, *J. Geophys. Res.*, *104*, 1541–1558, doi:10.1029/1998JC900035.

Balch, W. M., H. R. Gordon, B. C. Bowler, D. T. Drapeau, and E. S. Booth (2005), Calcium carbonate measurements in the surface global ocean based on Moderate-Resolution Imaging Spectroradiometer data, *J. Geophys. Res.*, *110*, C07001, doi:10.1029/2004JC002560.

Banse, K. (1991), Rates of phytoplankton cell division in the field and in iron enrichment experiments, *Limnol. Oceanogr.*, *36*, 1886–1898.

Behrenfeld, M. J., and E. Boss (2003), The beam attenuation to chlorophyll ratio: an optical index of phytoplankton photoacclimation in the surface ocean?, *Deep Sea Res., Part I*, *50*, 1537–1549, doi:10.1016/j.dsr.2003.09.002.

Behrenfeld, M. J., and E. Boss (2006), Beam attenuation to chlorophyll concentration as alternative indices of phytoplankton biomass, *J. Mar. Res.*, *64*, 431–451, doi:10.1357/002224006778189563.

Behrenfeld, M. J., and P. G. Falkowski (1997), Photosynthetic rates derived from satellite-based chlorophyll concentration, *Limnol. Oceanogr.*, *42*, 1–20.

Behrenfeld, M. J., E. Maranon, D. A. Siegel, and S. B. Hooker (2002), A photoacclimation and nutrient based model of light-saturated photosynthesis for quantifying ocean primary production, *Mar. Ecol. Prog. Ser.*, *228*, 103–117, doi:10.3354/meps228103.

Behrenfeld, M. J., E. Boss, D. A. Siegel, and D. M. Shea (2005), Carbon-based ocean productivity and phytoplankton physiology from space, *Global Biogeochem. Cycles*, *19*, GB1006, doi:10.1029/2004GB002299.

Behrenfeld, M. J., K. Worthington, R. M. Sherrell, F. Chavez, P. Strutton, M. McPhaden, and D. M. Shea (2006), Controls on productivity across the tropical Pacific ocean revealed through nutrient stress diagnostics, *Nature*, *442*, doi:10.1038/nature05083.

Bishop, J. (1999), Transimissometer measurements of POC, *Deep Sea Res., Part I*, *46*, 353–369, doi:10.1016/S0967-0637(98)00069-7.

Boyd, P. W., et al. (2000), A mesoscale phytoplankton bloom in the polar Southern Ocean stimulated by iron fertilization, *Nature*, *407*, 695–702, doi:10.1038/35037500.

Carr, M. E., et al. (2006), A comparison of global estimates of marine primary production from ocean color, *Deep Sea Res., Part II*, *53*, 741–770.

Clancy, R. M., and W. D. Sadler (1992), The Fleet Numerical Oceanography Center suite of oceanographic models and products, *Weather Forecasting*, *7*, 307–327.

Cloern, J. E., C. Grenz, and L. Vidergar-Lucas (1995), An empirical model of the phytoplankton chlorophyll:carbon ratio: The conversion factor between productivity and growth rate, *Limnol. Oceanogr.*, *40*, 1313–1321.

Conkright, M. E., H. E. Garcia, T. D. O'Brien, R. A. Locarnini, T. P. Boyer, C. Stephens, and J. I. Antonov (2002), *World Ocean Atlas 2001*, vol. 4, *Nutrients*, edited by S. Levitus, *NOAA Atlas NESDID 52*, 392 pp., U.S. Gov. Print. Off., Washington, D. C.

Cullen, J. J. (1982), The deep chlorophyll maximum: Comparing vertical profiles of chlorophyll, *Can. J. Fish. Aquat. Sci.*, *39*, 791–803.

de Baar, H. J. W., and P. W. Boyd (1999), *The Dynamic Ocean Carbon Cycle: A Midterm Synthesis of the Joint Global Ocean Flux Study*, edited by R. B. Hanson, H. W. Ducklow, and J. G. Field, chap. 4, pp. 61–140, Int. Geosphere Biosphere Programme Book Ser., Cambridge Univ. Press, Cambridge, UK.

Doney, S. C., D. M. Glover, S. J. McCue, and M. Fuentes (2003), Mesoscale variability of Sea-Viewing Wide Field-of-View Sensor (SeaWiFS) satellite ocean color: Global patterns and spatial scales, *J. Geophys. Res.*, *108*(C2), 3024, doi:10.1029/2001JC000843.

Durand, M. D., R. J. Olson, and S. W. Chisholm (2001), Phytoplankton population dynamics at the Bermuda Atlantic Time-series Station in the Sargasso Sea, *Deep Sea Res., Part II*, *48*, 1983–2003, doi:10.1016/S0967-0645(00)00166-1.

Falkowski, P. G., and J. La Roche (1991), Acclimation to spectral irradiance in algae, *J. Phycol.*, *27*, 8–14, doi:10.1111/j.0022-3646.1991.00008.x.

Fennel, K., and E. Boss (2003), Subsurface maxima of phytoplankton and chlorophyll: Steady state solutions from a simple model, *Limnol. Oceanogr.*, *48*, 1521–1534.

Flynn, K. J. (2001), A mechanistic model for describing dynamic multi-nutrient, light, temperature interactions in phytoplankton, *J. Plankton Res.*, *23*, 977–997, doi:10.1093/plankt/23.9.977.

Geider, R. J. (1987), Light and temperature dependence of the carbon to chlorophyll ration in microalgae and cyanobacteria: Implications for physiology and growth of phytoplankton, *New Phytol.*, *106*, 1–34, doi:10.1111/j.1469-8137.1987.tb04788.x.

Geider, R. J., H. L. MacIntyre, and T. M. Kana (1996), A dynamic model of photoadaptation in phytoplankton, *Limnol. Oceanogr.*, *41*, 1–15.

Geider, R. J., H. L. MacIntyre, and T. Kana (1998), A dynamic regulatory model of phytoplanktonic acclimation to light, nutrients, and temperature, *Limnol. Oceanogr.*, *43*, 679–694.

Goericke, R., and N. A. Welschmeyer (1998), Response of Sargasso Sea phytoplankton biomass, growth rates and primary production to seasonally varying physical forcing, *J. Plankton Res.*, *20*, 2223–2249, doi:10.1093/plankt/20.12.2223.

Gordon, H. R., and A. Morel (1983), Remote assessment of ocean color for interpretation of satellite visible radiometry, in *Lecture Notes on Coastal and Estuarine Studies*, edited by R. T. Barber et al., pp. 1–44, Springer, New York.

Jones, D. R., D. M. Karl, and E. A. Laws (1996), Growth rates and production of heterotrophic bacteria and phytoplankton in the North Pacific subtropical gyre, *Deep Sea Res., Part I*, *43*, 1567–1580, doi:10.1016/S0967-0637(96)00079-9.

Karl, D. M., and R. Lukas (1996), The Hawaii Ocean Time-series (HOT) program: Background, rationale and field implementation, *Deep Sea Res., Part II*, *43*, 129–156, doi:10.1016/0967-0645(96)00005-7.

Karl, D. M., R. R. Bidigare, and R. M. Letelier (2001), Long-term changes in plankton community structure and productivity in the North Pacific Gyre: The domain shift hypothesis, *Deep Sea Res., Part II*, *48*, 1449–1470, doi:10.1016/S0967-0645(00)00149-1.

Kitchen, J., and R. Zaneveld (1990), On the noncorrelation of the vertical structure of light scattering and chlorophyll a in case I waters, *J. Geophys. Res.*, *95*, 20,237–20,246, doi:10.1029/JC095iC11p20237.

Laws, E. A., and T. T. Bannister (1980), Nutrient- and light-limited growth of *Thalassiosira fluviatilis* in continuous culture, with implications for phytoplankton growth in the ocean, *Limnol. Oceanogr.*, *25*, 457–473.

Letelier, R. M., R. R. Bidigare, D. V. Hebel, M. Ondrusek, C. D. Winn, and D. M. Karl (1993), Temporal variability of phytoplankton community structure based on pigment analysis, *Limnol. Oceanogr.*, *38*, 1420–1437.

Loisel, H., E. Bosc, D. Stramski, K. Oubelkheir, and P.-Y. Deschamps (2001), Seasonal variability of the backscattering coefficient in the Mediterranean Sea on satellite SeaWiFS imagery, *Geophys. Res. Lett.*, *28*, 4203–4206, doi:10.1029/2001GL013863.

Loisel, H., J.-M. Nicolas, A. Sciandra, D. Stramski, and A. Poteau (2006), Spectral dependency of optical backscattering by marine particles from satellite remote sensing of the global ocean, *J. Geophys. Res.*, *111*, C09024, doi:10.1029/2005JC003367.

Longhurst, A., S. Sathyendranath, T. Platt, and C. Caverhill (1995), An estimate of global primary production in the ocean from satellite radiometer data, *J. Plankton Res.*, *17*, 1245–1271, doi:10.1093/plankt/17.6.1245.

MacIntyre, H. L., T. M. Kana, T. Anning, and R. J. Geider (2002), Photoacclimation of photosynthesis irradiance response curves and photosynthetic pigments in microalgae and cyanobacteria, *J. Phycol.*, *38*, 17–38, doi:10.1046/j.1529-8817.2002.00094.x.

Marañon, E. (2005), Phytoplankton growth rates in the Atlantic subtropical gyres, *Limnol. Oceanogr.*, *50*, 299–310.

Maritorena, S., D. A. Siegel, and A. R. Peterson (2002), Optimization of a semianalytical ocean color model for global-scale applications, *Appl. Opt.*, *41*, 2705–2714, doi:10.1364/AO.41.002705.

McClain, C. R., M. L. Cleave, G. Feldman, W. Gregg, S. Hooker, and N. Kuring (1998), Science quality SeaWiFS data for global biosphere research, *Sea Technol.*, *39*, 10–16.

McGillicuddy, D. J., and A. R. Robinson (1997), Eddy-induced nutrient supply and new production in the Sargasso Sea, *Deep Sea Res., Part I*, *44*, 1427–1450, doi:10.1016/S0967-0637(97)00024-1.

Moore, J. K., S. C. Doney, D. M. Glover, and I. Y. Fung (2001), Iron cycling and nutrient-limitation patterns in surface waters of the world ocean, *Deep Sea Res., Part II*, *49*(1–3), 463–507, doi:10.1016/S0967-0645(01)00109-6.

Morel, A., and J.-F. Berthon (1989), Surface pigments, algal biomass profiles, and potential production of the euphotic layer: Relationships reinvestigated in view of remote-sensing applications, *Limnol. Oceanogr.*, *34*, 1545–1562,.

Morel, A., and S. Maritorena (2001), Bio-optical properties of oceanic waters: A reappraisal, *J. Geophys. Res.*, *106*, 7163–7180,doi:10.1029/2000JC000319.

Mueller, J. L., et al. (2002), Ocean optics protocols for satellite ocean color sensor validation, revision 3, *NASA Technical Memo 210004*, vol. 1–2, edited by J. L. Mueller and G. S. Fargion, pp. 123–127, NASA Goddard Space Flight Cent., Greenbelt, Md.

Nelson, N. B., D. A. Siegel, and A. F. Michaels (1998), Seasonal dynamics of colored dissolved material in the Sargasso Sea, *Deep Sea Res., Part I*, *45*, 931–957, doi:10.1016/S0967-0637(97)00106-4.

O'Reilly, J. E., et al. (2000), SeaWiFS postlaunch calibration and validation analyses, part 3, *NASA Tech. Memo. 2000-206892*, vol. 11, edited by S. B. Hooker and E. R. Firestone, pp. 1–49, NASA Goddard Space Flight Cent., Greenbelt, Md.

Ricchiazzi, P., S. R. Yang, C. Gautier, and D. Sowle (1998), SBDART: A research and teaching software tool for plane-parallel radiative transfer in the Earth's atmosphere, *Bull. Am. Meteorol. Soc.*, *79*, 2101–2114, doi:10.1175/1520-0477(1998)079<2101:SARATS>2.0.CO;2.

Siegel, D. A., and A. F. Michaels (1996), Quantification of non-algal light attenuation in the Sargasso Sea: Implications for biogeochemistry and remote sensing, *Deep Sea Res., Part II*, *43*, 321–345, doi:10.1016/0967-0645(96)00088-4.

Siegel, D. A., D. J. McGillicuddy, and E. A. Fields (1999), Mesoscale eddies, satellite altimetry, and new production in the Sargasso Sea, *J. Geophys. Res.*, *104*, 13,359–13,379, doi:10.1029/1999JC900051.

Siegel, D. A., et al. (2001), Bio-optical modeling of primary production on regional scales: The Bermuda Bio-Optics Project, *Deep Sea Res., Part II*, *48*, 1865–1896, doi:10.1016/S0967-0645(00)00167-3.

Steinberg, D. K., C. A. Carlson, N. R. Bates, R. J. Johnson, A. F. Michaels, and A. H. Knap (2001), Overview of the US JGOFS Bermuda Atlantic Time-series Study (BATS): A decade-scale look at ocean biology and biogeochemistry, *Deep Sea Res., Part II*, *48*, 1405–1447, doi:10.1016/S0967-0645(00)00148-X.

Stramski, D., and D. Kiefer (1991), Light scattering by microorganisms in the open ocean, *Prog. Oceanogr.*, *28*, 343–383, doi:10.1016/0079-6611(91)90032-H.

Stramski, D., R. A. Reynolds, M. Kahru, and B. G. Mitchell (1999), Estimation of particulate organic carbon in the ocean from satellite remote sensing, *Science*, *285*, 239–242, doi:10.1126/science.285.5425.239.

Stramski, D., E. Boss, D. Bogucki, and K. J. Voss (2004), The role of seawater constituents in light backscattering in the ocean, *Prog. Oceanogr.*, *61*, 27–56, doi:10.1016/j.pocean.2004.07.001.

Vaillancourt, R. D., C. W. Brown, R. R. Guillard, and W. M. Balch (2004), Light backscattering properties of marine phytoplankton: Relationships to cell size, chemical composition and taxonomy, *J. Plankton Res.*, *26*(2), 191–212, doi:10.1093/plankt/fbh012.

Werdell, P. J., and S. W. Bailey (2005), An improved in-situ bio-optical data set for ocean color algorithm development and satellite data product validation, *Remote Sens. Environ.*, *98*, 122–140, doi:10.1016/j.rse.2005.07.001.

Winn, C. D., L. Campbell, J. R. Christian, R. M. Letelier, D. V. Hebel, J. E. Dore, L. Fujieki, and D. M. Karl (1995), Seasonal variability in the phytoplankton community of the North Pacific Subtropical Gyre, *Global Biogeochem. Cycles*, *9*, 605–620, doi:10.1029/95GB02149.

M. J. Behrenfeld and T. Westberry, Department of Botany and Plant Pathology, Oregon State University, 2082 Cordley Hall, Corvallis, OR 93106-3060, USA. (toby.westberry@science.oregonstate.edu)

E. Boss, School of Marine Sciences, University of Maine, 458 Aubert Hall, Orono, ME 04469, USA.

D. A. Siegel, Institute for Computational Earth System Science, University of California, Santa Barbara, CA 93106-3060, USA.